

AD619988

NRL Report 6257

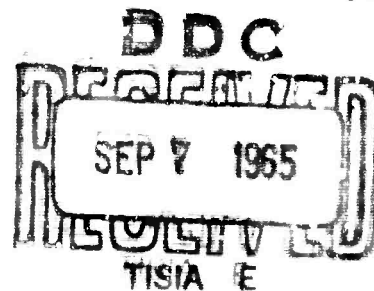
Dynamic Effects Arising from High-Speed Solidification

M. E. GLICKSMAN

*Metal Physics Branch
Metallurgy Division*

June 9, 1965

CITATION RESPONSE			
FOR FURTHER INFORMATION		TECHNICAL AND	
Hardcopy		A VON	
\$2.00	\$0.50	2.5 pp	ed
ARCHIVE COPY			



U.S. NAVAL RESEARCH LABORATORY
Washington, D.C.

DYNAMIC EFFECTS ARISING FROM HIGH-SPEED SOLIDIFICATION

INTRODUCTION

Most theories of crystal growth have dealt more or less directly with fundamental considerations such as atomic rearrangement, energy transfer, and defect structure at a solid-vapor or solid-liquid interface. Whereas this local (i.e., microscopic) viewpoint has led to considerable success in interpreting the kinetics and morphology of crystal growth, other aspects of crystallization exist which are less amenable to interpretations based on a strictly local approach and, therefore, have resisted even qualitative prediction and analysis.

Anomalous nucleation processes, cavitation, acoustical noise generation, and other dynamic effects associated with rapid crystal growth are subjects of current interest which, at present, have not been satisfactorily treated by theory. The intent of this paper is to account for the origin of these effects using an analysis of the macroscopic mechanics of a finite, metallic system undergoing rapid solidification. Some new experiments will be discussed which support critical areas of the theoretical analysis; in addition, an attempt will be made at reinterpreting some published data in the area of high-speed solidification utilizing the theoretical results developed here.

Almost without exception, conjugate solid-liquid phases differ in mass density by a small but significant amount. The viewpoint to be evolved here is that, during crystal growth, the active portions of the solid/liquid interface may be considered as a traveling front across which exist steep gradients in the mass density. Studies of the dynamical implications of mass-density gradients in motion during a phase change have been made by Chambré (1) and, more recently, by Horvay (2). Both Chambré's analysis and the more rigorous, comprehensive analysis by Horvay treated the cases of finite and semi-infinite solid-phase bodies growing in an infinite system. However, as will be subsequently shown, certain of the dynamical effects observed during crystal growth can be most easily interpreted from an analysis of a finite, or bounded, system undergoing a rapid phase change involving convective mass transfer.

THEORY

Approach

The aim of the following analysis is to obtain a description of the extrinsic mechanical behavior of a solidifying system in terms of intrinsic parameters which are related to the phase transformation occurring. Specifically, a model of dendritic crystallization will be analyzed using nonrigid-body mechanics to arrive at the equations of motion for the mass center of a finite, solidifying system. First, the position, velocity, and acceleration of the center of mass will be determined for a reasonable, yet tractable, growth morphology. This formulation will be largely kinematical in nature, and the equations which result will be expressed in terms of the intrinsic properties of the crystallizing body, i.e., the temperature, mass density, thermal constants, and dendrite velocity. In the second portion of the analysis, purely external considerations, such as ambient pressure, crucible wall effects, system constraints, etc., will be evoked in the application of Newton's laws, from which the required dynamical predictions will be made.

Model

Figure 1 illustrates a simple, bounded system composed of a thermally isolated mass (M_0) of molten metal which initially is uniformly supercooled an amount ΔT and is constrained by "ingot" walls and gravity to the shape of a right-circular cylinder of radius R and height h_0 . At time $t = 0$, growth of the solid phase is initiated, on the z axis, starting at the plane $z = 0$; moreover, the rapidly forming mass of dendritic crystals grows, on the average, with a constant tip speed (v) in the form of an expanding, spherically capped zone. The average position of the tips of the expanding dendritic mass at a later time (t) is given by the coordinate surface $r = r(t)$. This surface will be referred to as the recalescence zone boundary and, while spatially coincident with the dendrite tips, it should not be confused with the topologically complex, true, solid/liquid interface. The region $0 \leq r \leq r(t)$, termed the recalescence zone, is composed of a two-phase mixture containing fine, branched dendritic crystals of mass density ρ_s , and recalesced, interdendritic liquid of mass density ρ_ℓ . The region above the spherically capped recalescence zone is occupied by the remaining, untransformed, supercooled melt, also of density ρ_ℓ .*

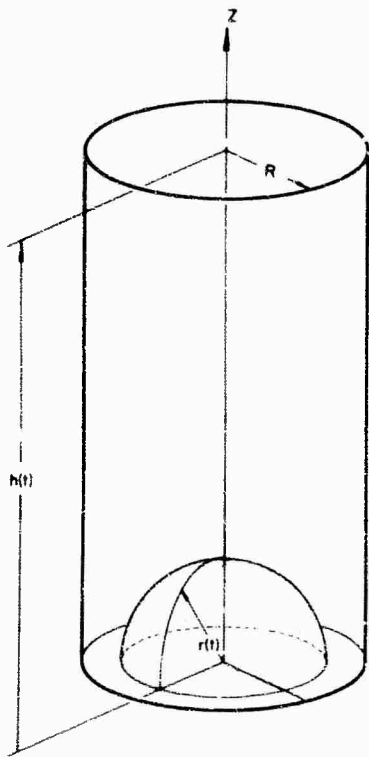


Fig. 1 - Model of a bounded, base-nucleated system undergoing rapid dendritic solidification. The base plane ($z=0$) is fixed relative to inertial axes, while the free surface [$z=h(t)$] is permitted to move parallel to the z axis.

In order to calculate the average mass density throughout this two-phase region, consider first the thermal energy balance within the recalescence zone. Assume that heat transfer from the zone to the confining walls can be neglected over the short time intervals required for recalescence of the entire system (usually 10^{-3} to 1 sec) and that the heat flowing to the supercooled liquid is, in essence, "captured" by the expanding zone which follows—indeed, is driven by—this heat diffusion. Assume further that the recalescence is complete, i.e., the equilibrium temperature has been restored throughout the zone by the release of the latent heat of solidification. This last assumption will cause a slight overestimation of the amount of solid phase in the zone because it neglects the temperature gradients which must exist near the zone boundary; fortunately, in metal systems these gradients are steep, short-ranged, and confined to the region near $r = r(t)$.

The mass-fraction f_s of solid phase that must solidify (dendritically) to liberate just enough latent heat λ to restore the zone temperature to the equilibrium value T_e is approximately given (3) by

$$f_s = \frac{c_p (T_e - T_\ell)}{\lambda}, \quad (1)$$

where c_p and T_ℓ are the specific heat and original (supercooled) temperature of the melt, respectively. We now define f_s in terms of the individual phase densities (ρ_s, ρ_ℓ) and phase volumes (V_s, V_ℓ) coexisting within the zone, namely,

$$f_s = \frac{V_s \rho_s}{V_s \rho_s + V_\ell \rho_\ell}, \quad (2)$$

which, when combined with Eq. (1) and the continuity statement $V_s + V_\ell = (2/3)\pi r(t)^3$ for $0 \leq r(t) \leq R$, yields an expression for the solid-phase volume given by

* The lack of distinction between the mass densities of the supercooled liquid phase and the recalesced, hotter, liquid phase is not significant here.

$$V_s = \frac{2}{3}\pi \left[\frac{f_s(\rho_s - \rho_l)}{\rho_s - f_s(\rho_s - \rho_l)} \right] r(t)^3. \quad (3)$$

The average zone density ρ_{sl} is defined here as

$$\rho_{sl} = \frac{V_s \rho_s + V_l \rho_l}{(2/3)\pi r(t)^3}. \quad (4)$$

Finally, when Eqs. (3) and (4) are combined with the continuity statement, given above, they yield the desired expression for the average zone density, namely,

$$\rho_{sl} = \left(1 + \frac{\beta}{\rho_s - \beta} \right) \rho_l, \quad (5)$$

where β is a solidification parameter defined by

$$\beta = f_s(\rho_s - \rho_l). \quad (6)$$

Kinematics of the Model

The location, along the z axis, of the center of mass for an n -body, heterogeneous system is specified by the center-of-mass coordinate z_{cm} defined by

$$z_{cm} = \frac{\sum_{i=1}^n \rho_i V_i' \bar{z}_i}{\sum_{i=1}^n \rho_i V_i'}, \quad (7)$$

where ρ_i , V_i' , \bar{z}_i are the mass density, volume, and z centroid of the individual constituent bodies of the system, respectively. For the system shown in Fig. 1, we conveniently choose the untransformed, supercooled liquid and the solid/liquid zone for the two constituent, nonrigid bodies and obtain for the centroid coordinate the relationship

$$z_{cm} = \frac{\rho_l V_l' \bar{z}_l + \rho_{sl} V_{sl}' \bar{z}_{sl}}{\rho_l V_l' + \rho_{sl} V_{sl}'}. \quad (8)$$

Expressions for the volumes and locations of the centroids can be written in terms of the spatial variables indicated in Fig. 1, keeping in mind that the free surface $z = h(t)$ can move to accommodate the volume changes which occur during freezing, and that the system's lower boundary is inertially fixed to the base plane $z = 0$. Also, note that any second-order effects arising from capillarity, viscosity, and compressibility have been entirely neglected. After some algebra, we thus find that the instantaneous position of the center of mass is given by

$$z_{cm} = \begin{cases} \frac{1}{2h_0} \left[h(t)^2 - \frac{r(t)^4}{2R^2} \left(\frac{\rho_{sl}}{\rho_l} - 1 \right) \right], & \text{for } 0 \leq r(t) \leq R, \end{cases} \quad (9a)$$

$$\begin{cases} \frac{1}{2h_0} \left[h(t)^2 - (r(t)^2 - R^2/2) \left(\frac{\rho_{sl}}{\rho_l} - 1 \right) \right], & \text{for } R \leq r(t) \leq \frac{\rho_l}{\rho_{sl}} h_0. \end{cases} \quad (9b)$$

The explicit dependences of $h(t)$ on $r(t)$ can be obtained by combining Eq. (5) with the following conservation-of-mass conditions:

$$\pi R^2 h_o \rho_\ell = \pi R^2 h(t) \rho_\ell + (2/3) \pi r(t)^3 (\rho_s \ell - \rho_\ell), \quad \text{for } 0 \leq r(t) \leq R, \quad (10a)$$

and

$$\pi R^2 h_o \rho_\ell = \pi R^2 h(t) \rho_\ell + (2/3) \pi \left(r(t)^3 - (r(t)^2 - R^2)^{3/2} \right) (\rho_s \ell - \rho_\ell), \quad (10b)$$

$$\text{for } R \leq r(t) \leq \frac{\rho_\ell}{\rho_s \ell} h_o;$$

this then yields

$$h(t) = h_o - \frac{2}{3} \left(\frac{\beta}{\rho_s - \beta} \right) \frac{r(t)^3}{R^2}, \quad \text{for } 0 \leq r(t) \leq R, \quad (11a)$$

and

$$h(t) = h_o - \frac{2}{3} \left(\frac{\beta}{\rho_s - \beta} \right) \left(\frac{r(t)^3 - (r(t)^2 - R^2)^{3/2}}{R^2} \right), \quad \text{for } R \leq r(t) \leq \frac{\rho_\ell}{\rho_s \ell} h_o. \quad (11b)$$

Equations (5) and (11), when substituted into Eq. (9), yield expressions for z_{cm} in terms of a single, dimensionless space variable $k = r(t)/R$. The required formulae for the velocity and acceleration of the system's center of mass can then be found by taking first and second time derivatives of z_{cm} , to which are applied the auxiliary conditions

$$\frac{dk}{dt} = \frac{v}{R} \quad (\text{where } v \text{ is the dendrite tip velocity})$$

and

$$\frac{d^2k}{dt^2} = 0 \quad (\text{during steady-state dendrite growth}).$$

This procedure yields for the velocity

$$\frac{dz_{cm}}{dt} = \begin{cases} \frac{R}{h_o} \left[k^3 - \frac{2h_o k^2}{R} + \frac{4}{3} \left(\frac{\beta}{\rho_s - \beta} \right) k^5 \right] \left(\frac{\beta}{\rho_s - \beta} \right) v, & \text{for } 0 \leq k \leq 1, & (12a) \\ \frac{R}{h_o} k \left[1 - \frac{2h_o}{R} (k - \sqrt{k^2 - 1}) + \left(\frac{\beta}{\rho_s - \beta} \right) g(k) \right] \left(\frac{\beta}{\rho_s - \beta} \right) v, & & (12b) \end{cases}$$

$$\text{for } 1 \leq k \leq \frac{h_o}{R} \left(1 - \frac{\beta}{\rho_s} \right), \quad (12b)$$

NAVAL RESEARCH LABORATORY

$$V_s = \frac{2}{3}\pi \left[\frac{f_s(\rho_s - \rho_\ell)}{\rho_s - f_s(\rho_s - \rho_\ell)} \right] r(t)^3. \quad (3)$$

The average zone density $\rho_{s\ell}$ is defined here as

$$\rho_{s\ell} = \frac{V_s \rho_s + V_\ell \rho_\ell}{(2/3)\pi r(t)^3}. \quad (4)$$

Finally, when Eqs. (3) and (4) are combined with the continuity statement, given above, they yield the desired expression for the average zone density, namely,

$$\rho_{s\ell} = \left(1 + \frac{\beta}{\rho_s - \beta} \right) \rho_\ell, \quad (5)$$

where β is a solidification parameter defined by

$$\beta \equiv f_s(\rho_s - \rho_\ell). \quad (6)$$

Kinematics of the Model

The location, along the z axis, of the center of mass for an n -body, heterogeneous system is specified by the center-of-mass coordinate z_{cm} defined by

$$z_{cm} = \frac{\sum_{i=1}^n \rho_i V'_i \bar{z}_i}{\sum_{i=1}^n \rho_i V'_i}, \quad (7)$$

where ρ_i , V'_i , \bar{z}_i are the mass density, volume, and z centroid of the individual constituent bodies of the system, respectively. For the system shown in Fig. 1, we conveniently choose the untransformed, supercooled liquid and the solid/liquid zone for the two constituent, nonrigid bodies and obtain for the centroid coordinate the relationship

$$z_{cm} = \frac{\rho_\ell V'_\ell \bar{z}_\ell + \rho_{s\ell} V'_{s\ell} \bar{z}_{s\ell}}{\rho_\ell V'_\ell + \rho_{s\ell} V'_{s\ell}}. \quad (8)$$

Expressions for the volumes and locations of the centroids can be written in terms of the spatial variables indicated in Fig. 1, keeping in mind that the free surface $z = h(t)$ can move to accommodate the volume changes which occur during freezing, and that the system's lower boundary is inertially fixed to the base plane $z = 0$. Also, note that any second-order effects arising from capillarity, viscosity, and compressibility have been entirely neglected. After some algebra, we thus find that the instantaneous position of the center of mass is given by

$$z_{cm} = \begin{cases} \frac{1}{2h_0} \left[h(t)^2 - \frac{r(t)^4}{2R^2} \left(\frac{\rho_{s\ell}}{\rho_\ell} - 1 \right) \right], & \text{for } 0 \leq r(t) \leq R, \end{cases} \quad (9a)$$

$$z_{cm} = \begin{cases} \frac{1}{2h_0} \left[h(t)^2 - \left(r(t)^2 - R^2/2 \right) \left(\frac{\rho_{s\ell}}{\rho_\ell} - 1 \right) \right], & \text{for } R \leq r(t) \leq \frac{\rho_\ell}{\rho_{s\ell}} h_0. \end{cases} \quad (9b)$$

The explicit dependences of $h(t)$ on $r(t)$ can be obtained by combining Eq. (5) with the following conservation-of-mass conditions:

$$\pi R^2 h_o \rho_\ell = \pi R^2 h(t) \rho_\ell + (2/3) \pi r(t)^3 (\rho_s \ell - \rho_\ell), \text{ for } 0 \leq r(t) \leq R, \quad (10a)$$

and

$$\pi R^2 h_o \rho_\ell = \pi R^2 h(t) \rho_\ell + (2/3) \pi \left(r(t)^3 - (r(t)^2 - R^2)^{3/2} \right) (\rho_s \ell - \rho_\ell), \quad (10b)$$

$$\text{for } R \leq r(t) \leq \frac{\rho_\ell}{\rho_s \ell} h_o;$$

this then yields

$$h(t) = h_o - \frac{2}{3} \left(\frac{\beta}{\rho_s - \beta} \right) \frac{r(t)^3}{R^2}, \text{ for } 0 \leq r(t) \leq R, \quad (11a)$$

and

$$h(t) = h_o - \frac{2}{3} \left(\frac{\beta}{\rho_s - \beta} \right) \left(\frac{r(t)^3 - (r(t)^2 - R^2)^{3/2}}{R^2} \right), \text{ for } R \leq r(t) \leq \frac{\rho_\ell}{\rho_s \ell} h_o. \quad (11b)$$

Equations (5) and (11), when substituted into Eq. (9), yield expressions for z_{cm} in terms of a single, dimensionless space variable $k = r(t)/R$. The required formulae for the velocity and acceleration of the system's center of mass can then be found by taking first and second time derivatives of z_{cm} , to which are applied the auxiliary conditions

$$\frac{dk}{dt} = \frac{v}{R} \text{ (where } v \text{ is the dendrite tip velocity)}$$

and

$$\frac{d^2k}{dt^2} = 0 \text{ (during steady-state dendrite growth)}$$

This procedure yields for the velocity

$$\frac{dz_{cm}}{dt} = \left\{ \begin{array}{l} \frac{R}{h_o} \left[k^3 - \frac{2h_o k^2}{R} + \frac{4}{3} \left(\frac{\beta}{\rho_s - \beta} \right) k^5 \right] \left(\frac{\beta}{\rho_s - \beta} \right) v, \text{ for } 0 \leq k \leq 1, \end{array} \right. \quad (12a)$$

$$\left\{ \begin{array}{l} \frac{R}{h_o} k \left[1 - \frac{2h_o}{R} (k - \sqrt{k^2 - 1}) + \left(\frac{\beta}{\rho_s - \beta} \right) g(k) \right] \left(\frac{\beta}{\rho_s - \beta} \right) v, \end{array} \right. \quad (12b)$$

$$\text{for } 1 \leq k \leq \frac{h_o}{R} \left(1 - \frac{\beta}{\rho_s} \right), \quad (12b)$$

where

$$g(k) = (4/3) \left(2k^4 - 2k^3 \sqrt{k^2 - 1} - 2k^2 + k \sqrt{k^2 - 1} + 1 \right),$$

and, for the acceleration

$$\frac{d^2 z_{cm}}{dt^2} = \begin{cases} \frac{1}{h_o} \left(3k^2 - \frac{4h_o k}{R} + \frac{20}{3} \left(\frac{\beta}{\rho_s - \beta} \right) k^4 \right) \left(\frac{\beta}{\rho_s - \beta} \right) v^2, & \text{for } 0 \leq k \leq 1, \\ \frac{1}{h_o} \left[1 - 2 \frac{h_o}{R} \left(k - \sqrt{k^2 - 1} - \frac{k}{\sqrt{k^2 - 1}} \right) + \left(\frac{\beta}{\rho_s - \beta} \right) \left(g(k) + k \frac{d}{dk} g(k) \right) \right] \left(\frac{\beta}{\rho_s - \beta} \right) v^2, & \end{cases} \quad (13a)$$

$$\text{for } 1 \leq k \leq \frac{h_o}{R} \left(1 - \frac{\beta}{\rho_s} \right). \quad (13b)$$

Equations (12) and (13) show that the system is subjected to accelerations even during steady-state dendrite growth (v constant), and that the directions of both the velocity and the acceleration of the center of mass depend upon the sign of β , i.e., whether the solid or liquid is the more dense phase.

It is also interesting to point out that if v be expressed by the usual empirical representation

$$v = A \Delta T^n \quad (n \sim 2)$$

(where ΔT is the degree of supercooling in the melt and A is a constant which depends on the material that is crystallizing), and be substituted into Eq. (13) along with the approximation*

$$\frac{\beta}{\rho_s - \beta} = \frac{c_p}{\lambda} \left(1 - \frac{\rho_l}{\rho_s} \right) \Delta T,$$

we obtain the semiempirical equation

$$\frac{d^2 z_{cm}}{dt^2} = \frac{A^2}{h_o} U(k) \frac{c_p}{\lambda} \left(1 - \frac{\rho_l}{\rho_s} \right) \Delta T^{2n+1}, \quad (14)$$

where $U(k)$ is a function depending primarily upon the geometrical details of the crystal growth, e.g., crucible shape and recalcence boundary shape. Equation (14) clearly indicates that the magnitude of the accelerations induced by solidification is extremely sensitive to the initial supercooling of the melt and to the difference from unity of the solid-to-liquid density ratio.

*This equation can be derived by substituting Eqs. (6) and (1) into the expression $\beta/(\rho_s - \beta)$, and then applying the approximation $\rho_s \gg (c_p/\lambda) \Delta T (\rho_s - \rho_l) \approx 0$.

Figure 2(a), derived from Eqs. (12a) and (12b), shows the variation of the (dimensionless) center-of-mass velocity with k , for several values of the aspect ratio h_0/R of the system. Figure 2(b) is also a plot of the dimensionless center-of-mass velocity derived from a model similar in all respects to the one discussed above, except that solidification has been nucleated on the free surface $z = h_0$ instead of on the base plane $z = 0$. The two models form an interesting comparison because, in the case of the base-nucleated solidification, the center-of-mass velocity exhibits a peak at $k = 1$ —with the velocity approaching zero at the completion of recalcence ($k = h_0/R$)—while the free-surface-nucleated model displays a monotonic increase in velocity.

Figure 3 shows the variation of dimensionless center-of-mass acceleration with k , for various aspect ratios, derived from Eqs. (13a) and (13b) for the base-nucleated model. This solidification mode is characterized by accelerations that build up rapidly in the early stages of recalcence ($k < 1$) then, after reversing direction and building up again to large magnitudes, rapidly decay to an almost constant value for the remainder of the rapid crystal growth. It will be shown that these growth-induced accelerations can be measured, and that the measurements provide the most direct experimental support of the kinematic analysis just given.

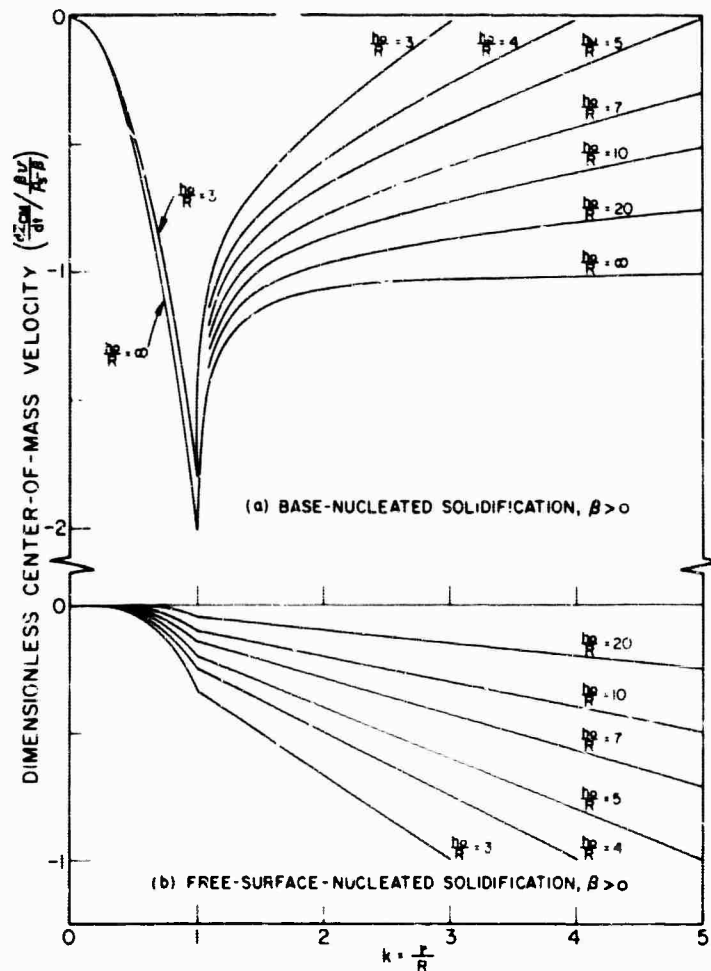
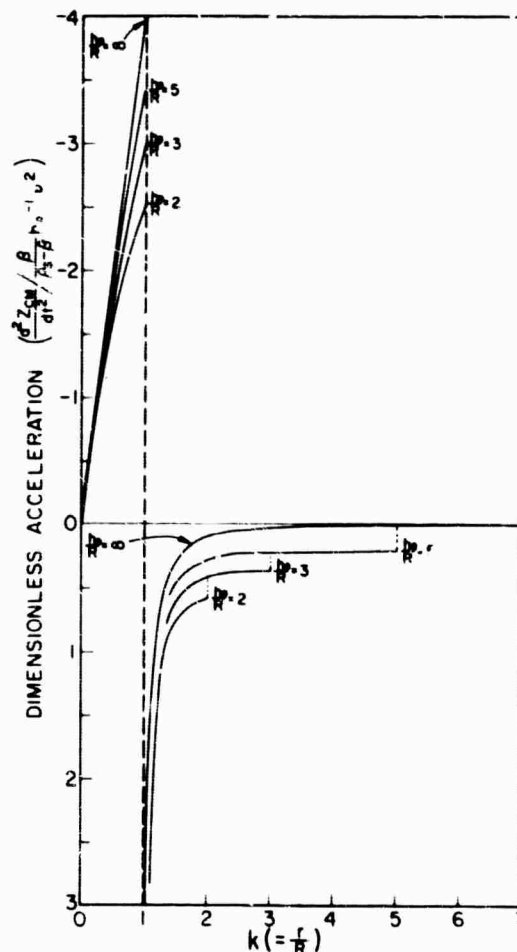


Fig. 2 - Theoretical variation of (dimensionless) center-of-mass velocity with (dimensionless) recalcence zone radius k for (a) base-nucleated solidification, and (b) free-surface-nucleated solidification

Fig. 3 - Theoretical variation of (dimensionless) center-of-mass acceleration with (dimensionless) recalescence zone radius k calculated for base-nucleated solidification and $\beta > 0$



Dynamical Analysis

Thus far, consideration has been limited to the question of what velocity and acceleration of the center of mass result from the specified configurational changes which accompany rapid, dendritic solidification when the participating phases differ in mass density. Inquiry is now made as to whether the kinematical accelerations can, in fact, be produced by the available forces which act on the system; furthermore, what limitations or modifications must be applied to the model to insure that the dynamical equations are satisfied?

Figure 4 is the free-body, z -axis force diagram for both the free-surface- and the base-nucleated models of recalescence. The three external forces which are shown are the weight $M_o g$, where g is the acceleration due to gravity; the external (ambient) pressure times the exposed area of the system, $\pi R^2 P_a$; and the reaction force f_z against the base of the system.

The net external force acting along the z axis, which is expressed by the vector sum

$$\sum_{ext} F_z = \pi R^2 P_a + M_o g + f_z, \quad (15)$$

is related to the center-of-mass acceleration by Newton's dynamical law

$$\sum_{ext} F_z = M_o \frac{d^2 z_{cm}}{dt^2}. \quad (16)$$

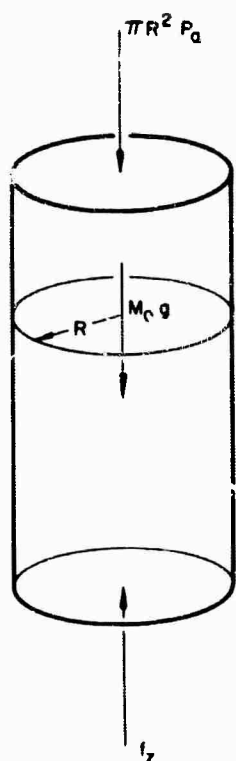


Fig. 4 - Free-body, z axis, force diagram indicating the forces for typical constraints, viz., gravity ($M_c g$), ambient pressure ($\pi R^2 P_a$), and contact support (f_z)

Since the weight and the force due to ambient pressure are constants, it is clear that, during solidification, the equality specified by Eq. (16) can be maintained only by an appropriate variation of f_z in the force sum given by Eq. (15). An alternative description of the variation of f_z is that recalescence produces a change in the net hydrostatic pressure within the freezing melt. Note, for instance, that $f_z / \pi R^2$ is the hydrostatic pressure across the plane $z = 0$.

The curves in Fig. 5 show the variation with k of the dynamic pressure reduction calculated from Eq. (16) for free-surface-nucleated growth in supercooled nickel. The acceleration values ($d^2 z_{cm} / dt^2$) in Eq. (16) were calculated from Eq. (13) for various degrees of supercooling using the constants for nickel listed in Table 1. The dashed horizontal line drawn through the pressure-reduction curves in Fig. 5 represents the maximum dynamic reduction in pressure that the system can support. This pressure cutoff is based on the fact that metallic melts generally will not wet an inert container and, therefore, will support only limited hydrostatic tension before fracture of the melt/container bond (cavitation) results. Indeed, the portions of the curves above the cutoff shown in Fig. 5 indicate that beyond about 175°C supercooling in nickel, the dynamic pressure reduction exceeds the total static pressure, and that significant levels of hydrostatic tension would result if no cutoff were imposed. Thus, the cutoff is a direct consequence of the limited forces which are available for producing accelerations of the center of mass with the system boundaries held "artificially" fixed. Furthermore, the solidification models must now be amended to include the onset of cavitation over the constrained surfaces of the melt when the total pressure drops just below zero. Choosing zero total pressure for the cavitation threshold neglects the additional hydrostatic tension usually required to overcome the nucleation barrier for bubble formation. This latter effect introduces no serious errors in the estimate for the cavitation pressure because the nucleation barrier for bubble formation is small for metallic liquids on nonwetted surfaces. Moreover, minute gas bubbles, which are usually distributed over melt/container interfaces, reduce the nucleation barrier by providing weak-spots (sites) for cavity formation.

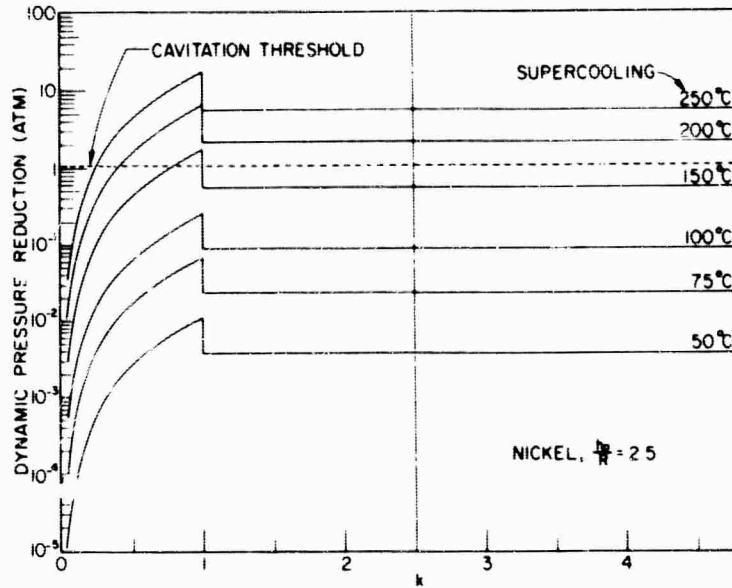


Fig. 5 - Decrease in hydrostatic pressure vs recalcence zone radius k (dimensionless), calculated for nickel at various levels of supercooling. The vertical, broken line indicates permissible extent of k for an aspect ratio h_0/R of 2.5. These data are for free-surface nucleation.

The kinematic analysis indicated earlier that free-surface-nucleated recalcence resulted in a monotonic increase, with k , of the center-of-mass velocity. A more useful result, which can be derived from that analysis with the dynamical considerations just given, is the dependence of the terminal, center-of-mass velocity on the initial degree of supercooling. The terminal velocity is a quantitative measure of the state of motion imparted to the system by the solidification process because the product of this velocity with the system mass M_0 gives the z -axis momentum accumulated at the cessation of recalcence. The overall increase in momentum which results from the action of the net, external forces during recalcence is easily calculated with the impulse equation

$$M_0 \dot{z}_{cm} = \int_0^{t_f \approx h_0/v} \sum_{ext} F_z dt, \quad (17)$$

where t_f is the total time of recalcence and \dot{z}_{cm} is the terminal, center-of-mass velocity. Equation (17) has been evaluated as a function of supercooling for free-surface-nucleated growth in nickel, again using the constants listed in Table 1. The values of \dot{z}_{cm} derived from Eq. (17) are plotted against the degree of supercooling in Fig. 6. The sharp drop in center-of-mass velocity at about 175°C results from the integrand in Eq. (17) becoming constant (limited net force), while the upper limit of the integral decreases monotonically with supercooling as $1/v$. Physically, however, this formulation indicates that it is the finite constraints which are responsible for the appearance of a critical degree of supercooling at which a maximum amount of mechanical energy is transferred to the system during rapid crystal growth. Furthermore, as shown in Fig. 6, the position and amplitude of the peak are relatively insensitive to the aspect ratio h_0/R of the system. It will be shown subsequently that the analysis given above provides a quantitative explanation for several phenomena observed during high-speed solidification.

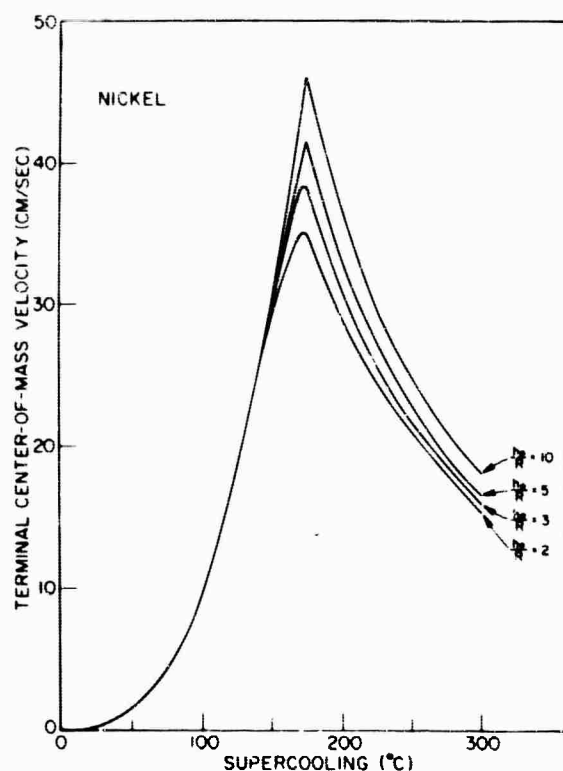


Fig. 6 - Terminal, center-of-mass velocity vs degree of supercooling, calculated for nickel. Free-surface-nucleation is assumed, along with a cavitation threshold of zero total pressure.

EXPERIMENTAL WORK

Confirmation of the Model

In the theory just presented, it was tacitly assumed that the morphology and motion of the recalescence boundary are predictable (on a macroscale) throughout the course of dendritic freezing. Furthermore, explicit assumptions were made that the recalescence boundary moves at a constant velocity during freezing, and that steady-state conditions are established quickly once growth starts. The foregoing assumptions were checked by means of high-speed cinematography.

High-speed cinematography is the best available technique for recording the surface details of rapid crystal growth, provided that adequate resolution of the boundary is realizable. In high-melting-point systems, such resolution can be achieved because the optical properties and the intensity of the radiation emitted by the supercooled melt preceding the solidification boundary differ from those of the latter dendritic crystals behind the boundary. In fact, Colligan and Bayles (4) used this technique to obtain cinematographs of solidification occurring in free-surface-nucleated, supercooled nickel specimens. Their results establish for nickel that, as assumed here, the recalescence boundary spreads out from the point of nucleation as a roughly spherical wave which travels at a constant velocity until the walls surrounding the specimen interfere with its motion. However, the solidification experiments in this work were performed on base-nucleated, supercooled bismuth specimens which were configured as cylinders with large aspect ratios ($h_0/R \sim 20$). In view of the differences between our specimens and those used in Colligan's work, it seemed desirable to confirm the applicability of the proposed model for our specimens. Unfortunately, the melting point of bismuth (272°C) is too low to allow our specimens to furnish emitted visible radiation for resolving the recalescence boundary.

The technique which was employed in photographing rapidly freezing bismuth is illustrated in Fig. 7. As shown, a thin, inert layer of flux (anhydrous stannous chloride) is

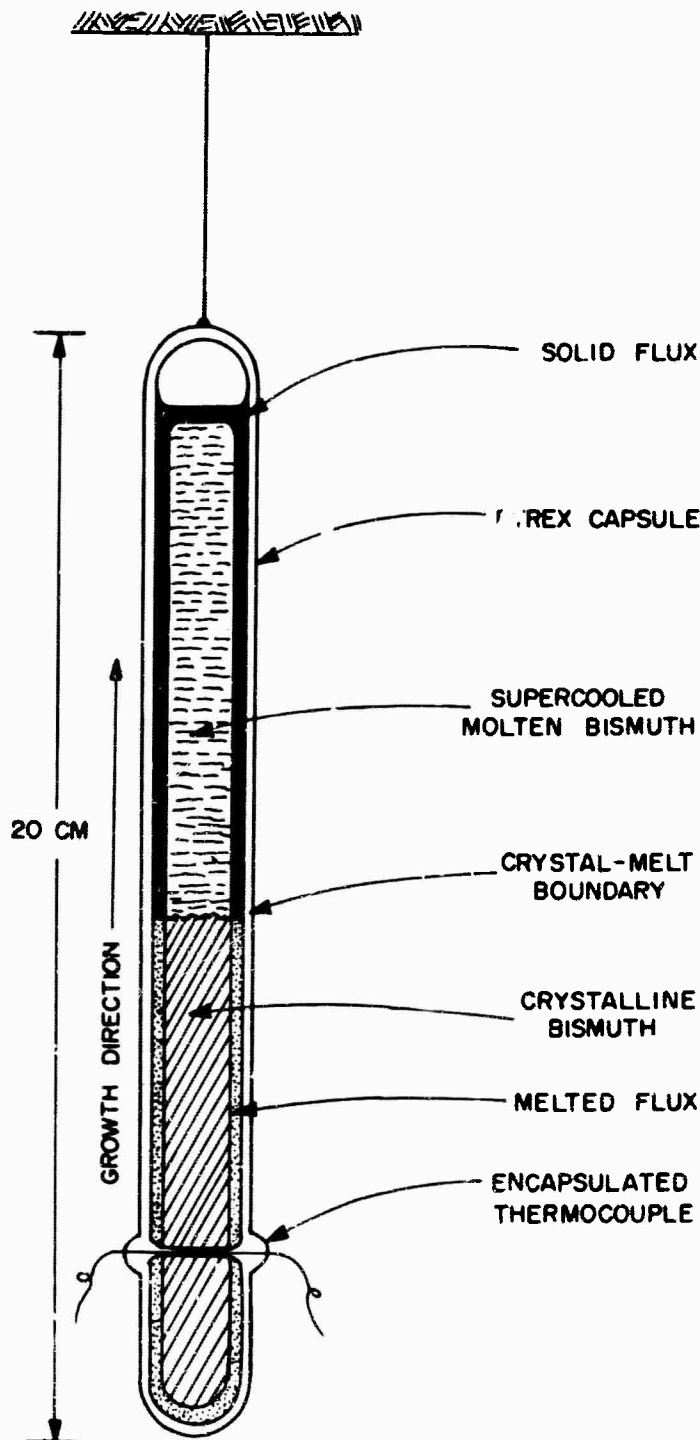


Fig. 7 - Schematic detail of bismuth solidification specimen used in cinematography experiments

entrapped between the molten bismuth specimen and the walls of the Pyrex viewing capsule. This flux has a melting point of 246°C and, normally, has solidified before the supercooled bismuth starts to crystallize. Once crystallization has commenced, the latent heat released at the recalescence boundary remelts the entrapped flux layer locally; moreover, the melting of the flux apparently produces enough change in the optical reflectivity at the flux/glass interface to supply the requisite resolution of the boundary's position.

Figure 8 is composed of a series of individual 16-mm frames, shown as high-contrast positives, selected from a full cinematographic sequence taken of bismuth crystals growing in a melt that was supercooled 66.6°C . The framing rate was 500 per second, and the exposure time was approximately $41\ \mu\text{sec}$ per frame. The white markers have been added to indicate the location of the boundary at the time specified for each photograph; for reference, the distance between the wire markers on the viewing capsule is 65 mm. Between 20 to 30 frames were required to span the event along the entire 140-mm path available for crystal growth. Figure 8 demonstrates that the phase transformation was base-nucleated, and that the growth front moved through the supercooled melt continuously from bottom to top. No isolated, secondary nucleation sites were ever observed ahead of the main boundary; this is consistent with the original assumption of a simple, expanding growth front. It should be noted, however, that metallographic examination of the specimens showed that the interior of most specimens was polycrystalline. This last observation is not easily reconciled with the assumed growth mode.

Figure 9 shows the displacement of the recalescence boundary measured as a function of time for two levels of melt supercooling. The linearity of these data supports the assumption that the recalescence boundary moves at a constant velocity during rapid growth, except, perhaps, for a short initial period following nucleation. Axial temperature gradients arising from end losses were doubtless present before nucleation; however, as indicated in Fig. 9, their influence on the dendrite velocity was barely detectable. Examination of the data points in Fig. 9 shows that only a slight, systematic drop in velocity occurred about midway through the growth period.

It was mentioned earlier that the growth-induced accelerations of the center of mass provide a sensitive, direct indication of the validity of the kinematical analysis. On that basis, acceleration-time profiles were obtained for several bismuth specimens of the type described by measuring the variation with time of the total axial force acting on the specimens during rapid crystallization. The apparatus used for these measurements is schematically illustrated in Fig. 10.

As shown in Fig. 10, the vertical component of the reaction force of the capsule against the specimen, along with a static load from the capsule, was transmitted through the suspension system to a piezoelectric force transducer. This apparatus provided an output signal which was proportional to the deviation of the instantaneous force from the statical value; moreover, the output voltage was also proportional to the net, vertical accelerations experienced by the specimen.

The transducer was constructed from two 1/2-in.-diam, 1/4-in.-thick wafers of Clevite PZT-5 ferroelectric ceramic. First, the ceramic wafers were electrically activated ("poled") parallel to their cylindrical axes in order to obtain a high, axial, electromechanical coupling coefficient. Then, two faces of common polarity were joined with a conductive epoxy cement. In this manner, a transducer was constructed which provided a vertical-force sensitivity of $11.2\ \mu\text{volt/dyne}$. The center-fed output signal from the transducer was coupled through low-capacitance cable to a unity-gain cathode follower stage, which provided an impedance match ($5 \times 10^9\ \text{ohm}$ input, $290\ \text{ohm}$ output) between the transducer and the readout oscilloscope. Overall, this apparatus provided flat frequency response from about 0.5 cps to the resonant frequency of the suspension system.

The procedure followed during each of these experiments consisted of: (a) heating the specimen capsule to $300\text{--}400^{\circ}\text{C}$ in order to completely melt and superheat the bismuth and flux; (b) coupling the capsule to the transducer, and then allowing the specimen to air-cool slowly; (c) monitoring the output signal from the encapsulated Pt-Pt, 10% Rh thermocouple with a potentiometric recorder to obtain the level of supercooling at which the specimen nucleated, and at which solidification took place; and (d) photographing the transient force-time signal displayed on the readout oscilloscope during recalescence of the specimen.

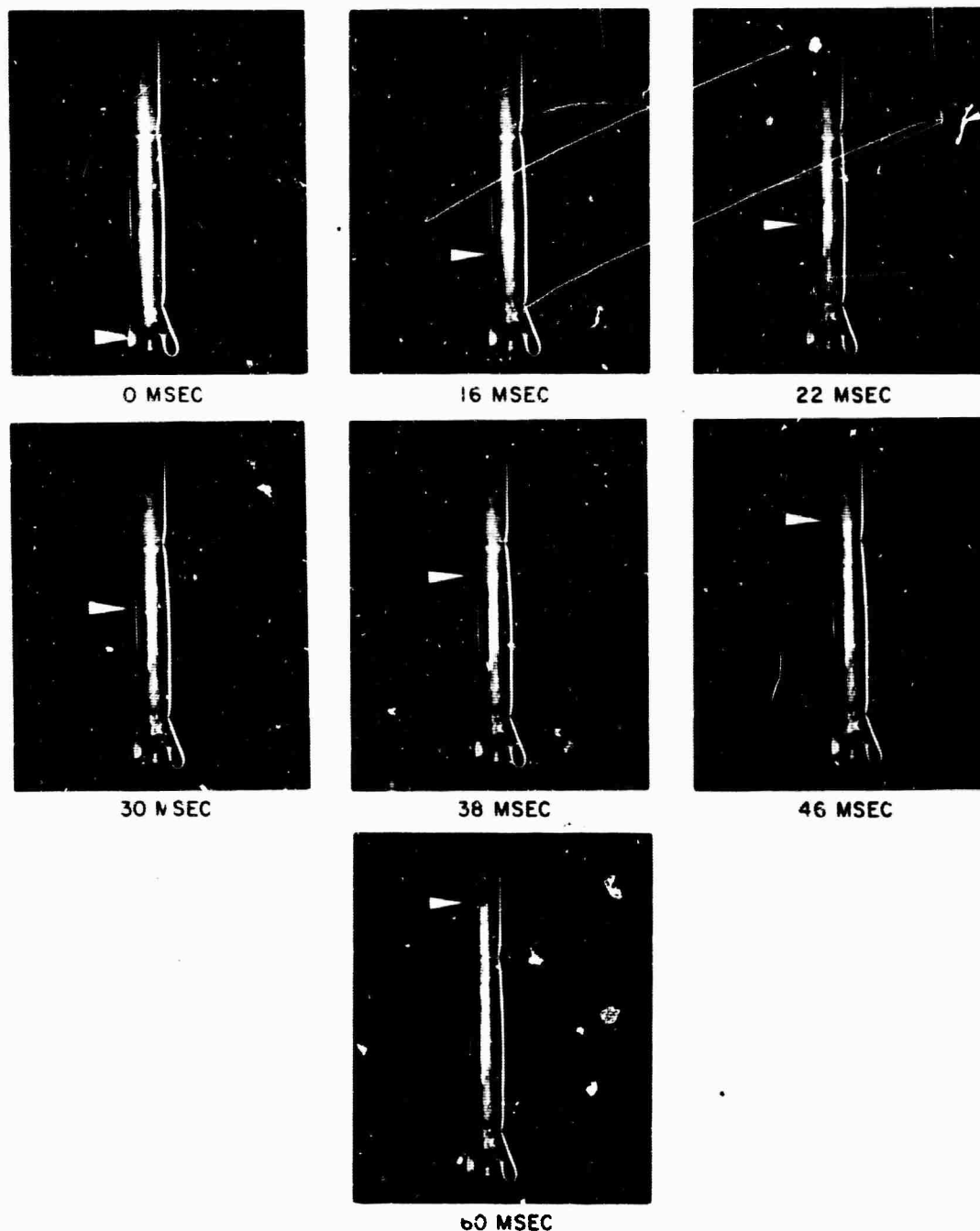


Fig. 8 - Cinematographic sequence of bismuth dendrites growing into a melt supercooled 66.6°C . Distance between wire markers is 65 mm; total growth path is 140 mm.

Figure 11 shows the acceleration-time variation measured during rapid solidification of a 1.3-cm. diam, 10-cm-long bismuth specimen, which was suspended from the transducer on a 0.6-cm-diam, 12-cm-long stainless steel rod. The data points were calculated from a set of force-time coordinates measured from the oscilloscope trace. The observed acceleration-time profile is in good qualitative agreement with that predicted from the kinematical analysis (cf., Figs. 3 and 11). The apparent disagreement in sign between the observed and predicted accelerations is attributable to the fact that, in the bismuth specimens, the solid phase was less dense than the liquid ($\beta < 0$), while in the theoretical

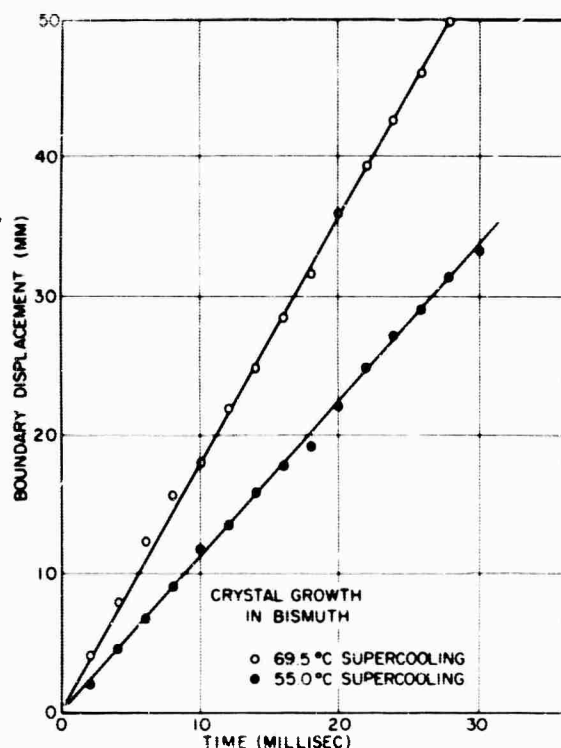


Fig. 9 - Recalescence boundary displacement vs time. The data were obtained from cinematography of bismuth specimens solidifying at two levels of supercooling.

calculations we assumed that the usual situation prevailed, viz., that the solid was more dense than the liquid ($\beta > 0$). The only significant feature that appeared on the oscilloscope trace and is omitted in Fig. 11 was a train of 1.8-kcps oscillations which occurred at the cessation of rapid freezing (beyond $t = 14$ msec in Fig. 11). These oscillations resulted from the excitation of resonant, elastic vibrations of the suspension system. Typically, these vibrations damped out over a period of about 15 msec, during which time the average acceleration of the system remained at zero; furthermore, since the vibrations are an extraneous effect introduced by the apparatus, no additional discussion of them will be given here.

Impulse Measurements

As shown earlier, the momentum or center-of-mass velocity depends primarily upon the configuration of the system, upon the mode of solidification, and upon the imposed mechanical constraints. Since it is the momentum acquired during recalescence that determines the mechanical activity of the specimen after recalescence, a quantitative measurement of growth-induced momentum was made (a) to prove that a portion of the transformation energy is transferred to the specimen as mechanical energy, (b) to show that solidifying specimens can experience a momentum change during rapid crystal growth, and (c) to evaluate the possibility of an interaction between the mechanical disturbances and the partially solidified structure.

While a measurement of the area beneath the experimental acceleration-time curves would, in principle, yield directly the velocity of the center of mass and the momentum, this method did not prove feasible. The major problem associated with integrating the acceleration-time curves was that it was difficult to confine the sharply peaked acceleration signals within the area of the oscilloscope screen and, at the same time, to maintain an adequate detection sensitivity. For instance, whereas sufficient signal resolution is provided in Fig. 11 for a reasonably accurate integration, the uncertainties which arise when estimating the areas under the missing peaks would subject the integration to errors large enough to vitiate the results.

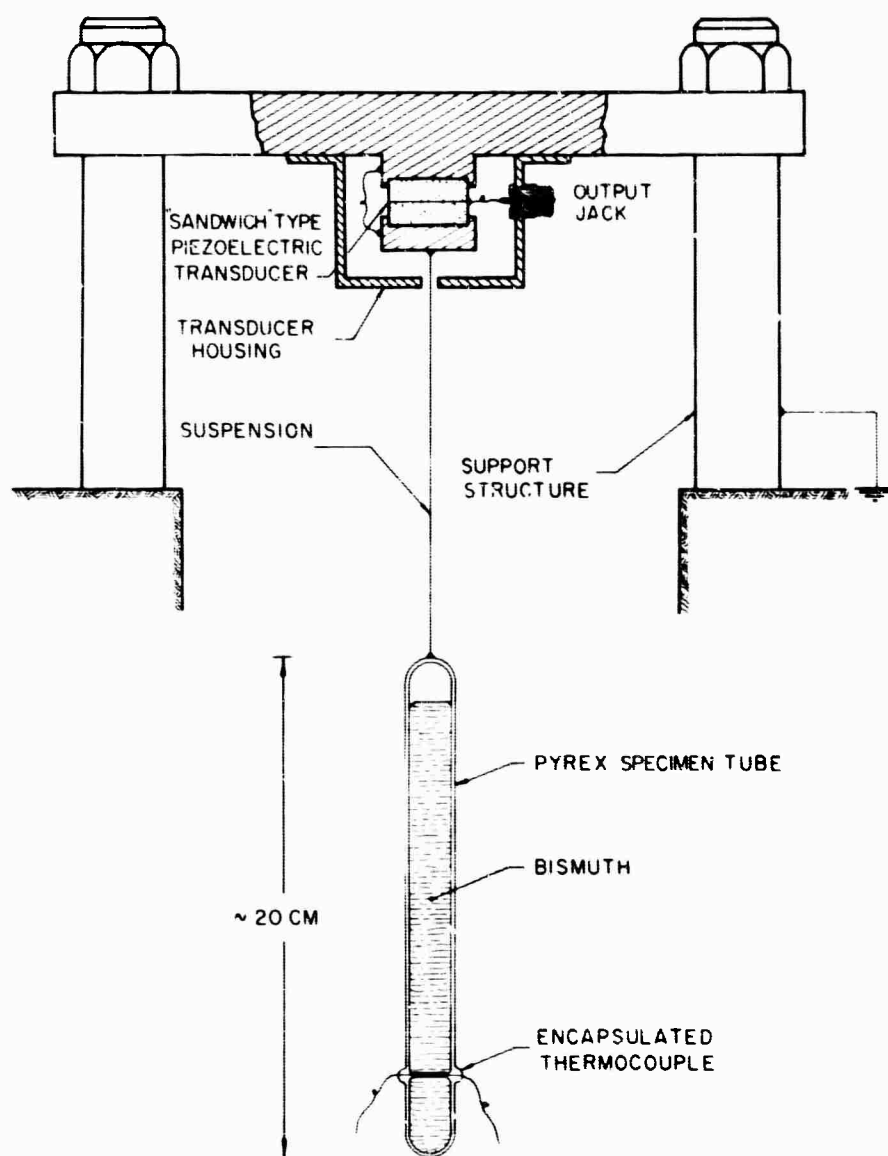


Fig. 10 - Schematic diagram of apparatus used to measure acceleration and velocity of bismuth specimens during solidification

The difficulties of detecting the momentum imparted to the specimens during recalcence were overcome by using a method which is based on the principle of the ballistic pendulum. The transducer suspension in the apparatus already described in Fig. 10 was modified in order to reduce its resonant frequency from several kilocycles per second—the frequency used previously for acceleration measurements—to approximately 20 cps. With the low-frequency suspension the apparatus behaved as a linear pendulum, integrating force impulses directed along the axis of the suspension. At the start of each experimental trial, the capsule containing the molten specimen was suspended from the transducer on a fine (0.075-mm-diam), carbon-steel wire approximately 34 cm long. Before nucleation occurred, precaution was always taken to cancel extraneous motions of the suspension, which are unavoidably introduced when attaching the specimen. The degree of supercooling sustained by the melt at the start of solidification was measured in the same fashion as described above for the acceleration measurements.

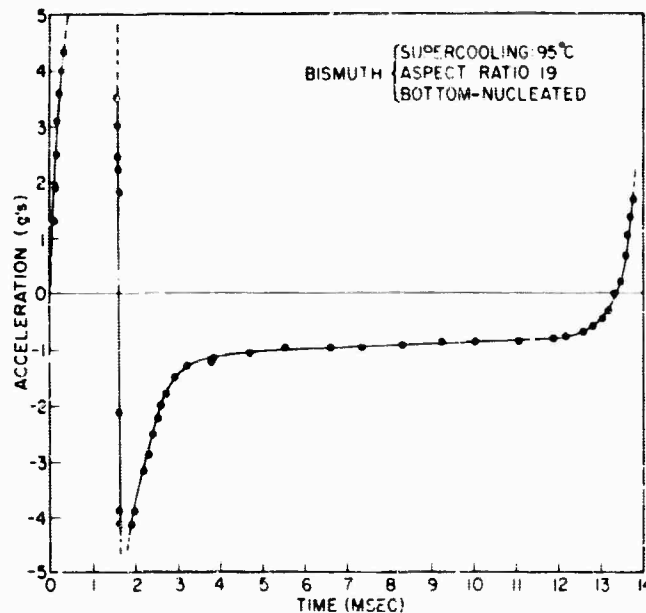


Fig. 11 - Acceleration-time profile measured during the solidification of a bottom-nucleated bismuth specimen (compare with Fig. 3)

When solidification finally occurred, the specimen was observed to oscillate at the resonant frequency of the suspension. The output signal recorded from the transducer was in the form of a slightly damped, voltage-time sinusoid which decreased to half its initial amplitude in about 3 sec. The signal amplitude was proportional to the periodic deviation from the static value of the instantaneous tension in the suspension wire.

The net momentum ΔJ acquired by the pendulum during recalescence of the specimen can be calculated from the oscilloscope record using the expression

$$\Delta J = \frac{T_{\max}}{2\pi\nu}, \quad (18)$$

where T_{\max} and ν are the maximum force amplitude and the frequency of the sinusoidal force-time signal, respectively. Equation (18) can be derived from the theory of simple harmonic oscillators if it is assumed that the duration of the impulse is short in comparison to the period of the pendulum. The accelerations shown in Fig. 3, although derived originally for a system with "inertial" boundary conditions, are also representative of the type of accelerations (or forces) which act on the pendulum system, except that a harmonic modifying function is not shown. As indicated in Fig. 3, when specimens have a large aspect ratio ($t_o/R > 10$), the large "high-frequency" forces in the range $0 \leq k \leq 1$ act impulsively on the pendulum, while the smaller, "low-frequency" forces beyond $k = 1$ contribute negligible net momentum to the pendulum. In effect, then, the pendulum selectively integrates the high-frequency components of the solidification-induced forces and, therefore, provides a measure of the maximum momentum of the system.

Figure 12 shows the results obtained from the pendulum measurements. The data in Fig. 12 were calculated from the measurements using Eq. (18) and are shown with velocity, instead of momentum, as the ordinate. Velocity was chosen as the ordinate because the velocity of the center-of-mass is proportional to the momentum, and yet it is independent of the mass of the particular specimen used to make the measurement. The curve which

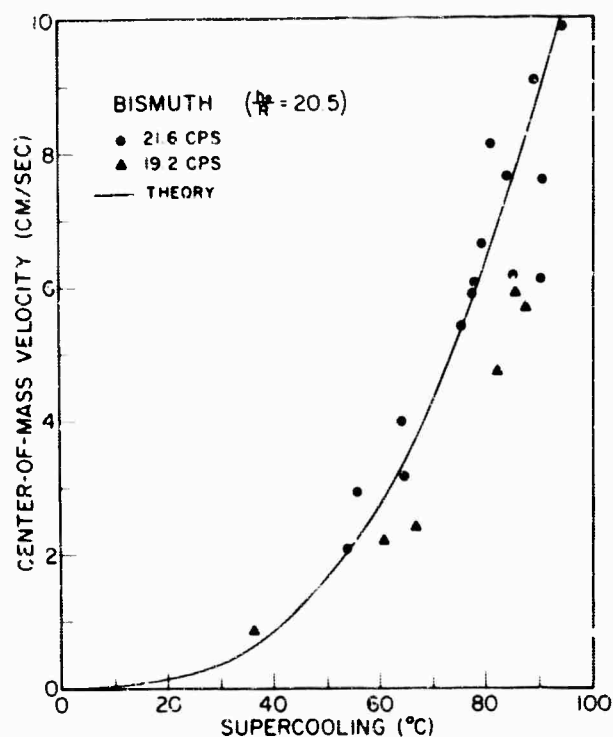


Fig. 12 - Center-of-mass velocity vs degree of supercooling. The data were obtained from pendulum measurements on solidifying bismuth.

appears in Fig. 12 was theoretically calculated from Eq. (12a) using the constants for bismuth listed in Table 1. Considering that there are no adjustable parameters in the theory, comparison between theory and experiment seems satisfactory within the uncertainties established by the scatter in the measurements and within the errors in the constants chosen for Table 1.

Table 1
Materials Constants Used for Dynamic Calculations

Material	Thermal Constants			Phase Densities		Growth Constants	
	T_c (°C)	λ (cal/gm)	C_p (cal/gm-°C)	ρ_s (gm/cm ³)	ρ_l (gm/cm ³)	A (cm/sec-°C)	n
Nickel	1453	73.8	0.157	8.30	7.95	0.28	1.8
Reference Source*	1	2	2†	1†	4,5	4†	4†
Bismuth	271	12.5	0.034	9.70	10.03	0.1	2
Reference Source*	1	2	3	3	3	6	6

* These numbers refer to the Table References given at the end of the present report.

† Calculated from source data given in the indicated Table Reference.

‡ From regular Reference listing at end of the present report

DISCUSSION

Introduction

In the previous sections devoted to theory and analysis, a framework was developed for understanding how some dynamic effects arise during the dendritic solidification of a metal. Experiments were then provided to check certain of the more mechanical aspects of the theoretical treatment. The limitations in both the theoretical and the experimental work stem from the choice of a transformation geometry which was contrived more for its mathematical tractability than for its wide applicability, and from some obviously oversimplified assumptions concerning the details of the thermal environment of an interacting mass of dendritic crystals growing in a supercooled melt.

A redeeming feature of this approach is that, notwithstanding the restrictive assumptions in the theory, the qualitative predictions of the analysis are often useful. A good example is an interpretation now to be given of some work done earlier by J.L. Walker (5). Walker's work involved a number of interesting experiments in which large samples (hundreds of grams) of nickel and cobalt were supercooled in varying amounts up to the degree of supercooling required for homogeneous nucleation. Two effects observed by Walker, which are of interest here, are the emission of audible noises from rapidly freezing melts, and a grain-size transition in nickel from normal, as-cast coarse grains (2 cm diam) to fine grains (0.01 cm diam) as the supercooling prior to solidification was increased beyond about 175°C.

Acoustical Disturbances

Acoustical disturbances in the form of audible "bumps" or clicks were reported by Walker (5), who first observed the recalescence of highly supercooled nickel specimens. Walker measured the magnitude of the disturbance by recording the signal amplitude generated by a phonograph cartridge coupled to a rigid probe which extended into the freezing nickel specimen. Figure 13 shows the variation with the degree of supercooling of the disturbance amplitude.

It appears likely that the disturbances which were detected in Walker's "phonograph cartridge" experiment were a manifestation of an impulsive interaction, via sound (pressure) waves, between the solidifying melt and the probe. A well-defined mechanical parameter which can be logically associated with these pressure disturbances is the momentum change or impulse between the melt and its surroundings. Furthermore, it can be shown from elastic theory* that pressure and impulse are related by

$$\Delta p_i = c_i \Delta J, \quad (19)$$

where Δp_i is the pressure-wave amplitude generated in a body during an impulsive interaction, c_i is the velocity of sound, and ΔJ is the momentum per unit volume transferred by the elastic wave from the solidifying body to its surroundings. Equation (19) shows that when impulsive momentum transfer generates pressure waves in a system, the amplitude of the pressure waves is proportional to the change in momentum density. Thus, Eq. (19) provides a basis for understanding the marked similarity between the disturbance data in Fig. 13 and the calculated velocity curves in Fig. 6. Both Figs. 6 and 13 represent the

*Equation (19) is an alternative form of the impulse equation (No. 261) given on p. 441 of "Theory of Elasticity," by S. Timoshenko and J.N. Goodier, New York: McGraw-Hill (1951).

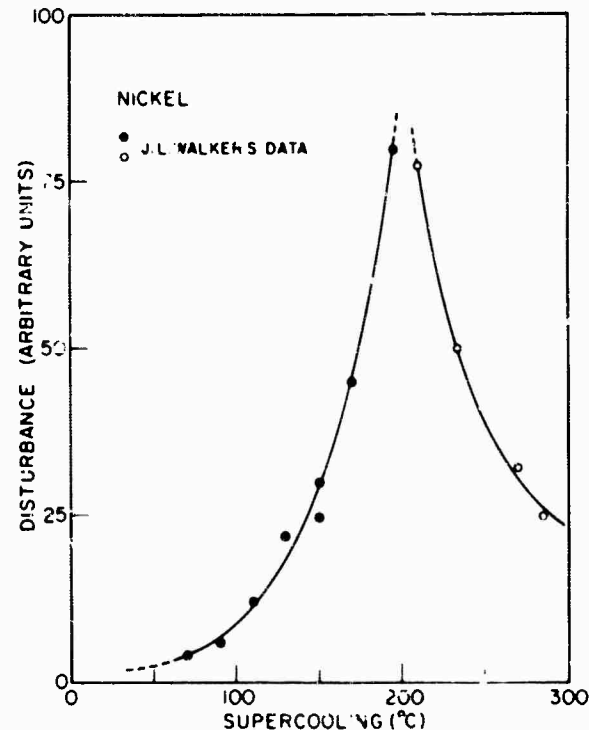


Fig. 13 - Acoustical disturbance amplitude (arbitrary units) vs degree of supercooling, scaled from J.L. Walker's data on nickel (6)

situation in which nickel specimens with aspect ratio of 2.5 froze dendritically from a nucleation point on the free surface of the melt. The relationship between the acoustical disturbances and the growth-induced, center-of-mass velocity (or momentum) can be placed on a more quantitative basis by comparing the functional variation of these quantities with the degree of supercooling prior to solidification.

Figure 14 shows a logarithmic plot of the disturbance data taken from Fig. 13 and a theoretical line with the slope predicted from Eq. (17). Although the data in Fig. 14 do not include the measurements occurring beyond the peak in Fig. 13, the correspondence between Walker's data (6) and the theoretically predicted slope is satisfactory.

The disturbance data that were obtained beyond the peak in Fig. 13 have not been treated quantitatively because, as explained in the section on dynamical analysis, cavitation effects must enter into the solidification process at levels of supercooling which approach the peak in the disturbance-supercooling curve. Because it is not yet possible to describe either the spatial distribution or the motion of the cavitation pockets which form on the constrained surfaces of the solidifying specimen, the analysis cannot, at present, be extended to rationalize quantitatively the disturbance data at levels of supercooling beyond about 175°C.

Cavitation Effects

Although no precise predictions can be offered concerning the behavior of solidifying systems after cavitation has occurred, some observations directly concerning cavitation can be explained, at least semiquantitatively.

From Fig. 5 we can predict that, in nickel, traces of cavitation might be in evidence at levels of supercooling as low as about 130°C. Also, the total volume of the cavitated pockets should increase with increased supercooling because, at higher levels of supercooling, a greater fraction of the solidification process occurs near zero hydrostatic pressure, i.e., occurs under conditions favorable for cavity formation.

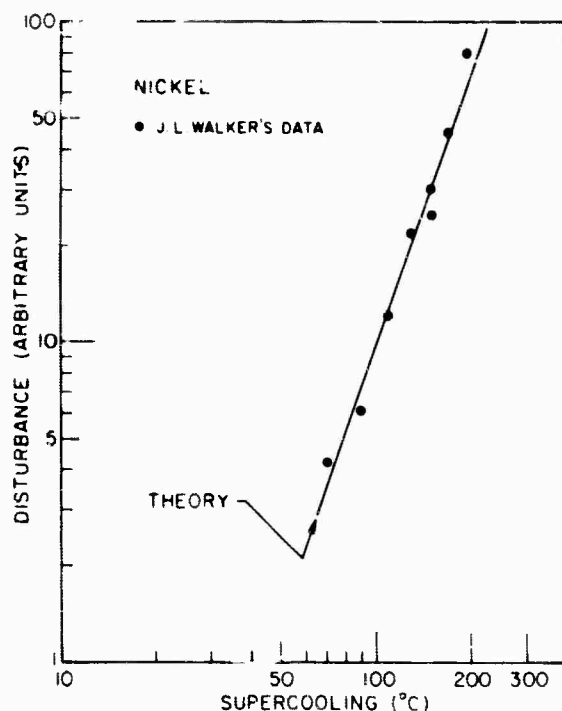


Fig. 14 - Logarithmic plot of acoustical disturbance amplitude (arbitrary units) vs degree of supercooling. The data points are scaled from J.L. Walker's data on nickel (6), and the line through the data is drawn with a slope predicted from theory [Eq. (17)].

The cavities formed by the dynamical reduction in hydrostatic pressure should be distributed as a myriad of small peckmarks on the constrained surfaces of the specimen. Furthermore, the position at which cavitation would most likely begin is at the cylindrical side walls adjacent to the free melt surface because, at that position, the hydrostatic pressure is lower than at other points on the melt/crucible interface. Figure 15 shows some pitlike surface formations distributed over the base of a 37-mm-diam ingot of cobalt that had sustained a supercooling of 226°C before solidifying. J.L. Walker (6) has observed similar surface markings in nickel ingots which were frozen from a highly supercooled condition, and B.J. Bayles (7) has observed surface cavities in rapidly solidified iron specimens.

Grain Size Transition

The sharp decrease in as-cast grain size with increased supercooling, which has been observed by Walker in nickel and cobalt, represents one of the most perplexing phenomena associated with high-speed solidification. Horvay has presented some interesting hydrodynamical arguments (2) which indicate that cavitation and enhanced nucleation can occur when the hydrostatic tension in the flow field ahead of an advancing dendritic crystal exceeds the fracture strength of the melt. Since the cohesive strength of a liquid metal under hydrostatic tension is of the order of 10^5 atm, it is clear that the dynamic effects now under consideration could not produce grain refinement by Horvay's mechanism. Nevertheless, several alternatives for explaining the grain-size transition are suggested by the present work.

The first explanation offered is that a collapse of some of the surface cavities early in the solidification process causes large, local pressure fluctuations which enhance the "classical" nucleation rate occurring in the untransformed, supercooled melt. The origin of this rate enhancement is the pressure-induced elevation of the solid-liquid equilibrium temperature, which may be predicted from the Clapeyron equation. A discussion of this mechanism has recently been given by Chalmers (8).

A second mechanism which must be considered is that of the collapse of the surface cavities at the termination of recalescence. When the surface cavities collapse—at least partial collapse must occur at the cessation of dendritic growth—a transient flow of molten metal will be established in the interdendritic channels throughout the specimen. The structure of a specimen just after recalescence is composed of fine (micron diameter), fragile, branched dendrites, which account for about 10 to 50 percent of the volume, and interdendritic melt near the equilibrium temperature, which accounts for the remainder. The presence of fluid flow in such an unstable structure could cause displacements and/or fracture of the dendritic skeleton which would produce a refinement in the final grain size. No enhancement of the nucleation rate is required for this mechanism.



Fig. 15 - Pitlike surface formations distributed over the base of a cobalt ingot which was supercooled 226°C before solidifying (photograph courtesy of Professor G.A. Colligan, private communication)

Finally, it appears possible that the impulses, which result when solidification-induced momentum is transferred from a specimen to its surroundings, can interact with the recalesced structure and produce grain refinement. Figure 16 shows the force impulse measured at the base of a crucible of solidifying bismuth. The specimen was supercooled about 85°C when solidification started. The measurements were performed in the same manner as described in the section on experimental work, except that the specimen was not suspended from the accelerometer but rested on an insulating plate to which was attached the force sensor. The photograph shows that the specimen was subjected to two groups of forces: The first group was composed of the solidification-induced forces which lasted about 40×10^{-3} sec, as indicated by the period τ ; the second group consisted of a train of powerful impulses resulting from the transfer, to and fro, of growth-induced momenta between the specimen and the support plate. Impulse pressures as large as 4.2×10^6 dyne/cm² have been measured in bismuth. The linear damping of a portion of the impulses in Fig. 16 indicates that the entire specimen of about 150 gm was subjected to nine or ten restitutive bounces on the support plate. Clearly, then, the evidence is strong for the presence, just after rapid growth ceases, of dendrite-damaging impact pressures. Lastly, it should be noted that the dynamic effects measured when supercooled bismuth solidifies are likely to be considerably milder than those encountered during the solidification of materials such as nickel, iron, or cobalt. The reason is that the maximum growth velocities which are attainable in supercooled bismuth are only about one tenth as large as those observed in the transition metals mentioned above.

SUMMARY AND CONCLUSIONS

A hypothesis has been proposed to explain the dynamical behavior of systems subjected to rapid, dendritic solidification. The theoretical conclusions, given next, were developed from a Newtonian analysis of the mass redistribution which occurs across a dendritic solidification front.

1. It was shown that even under the conditions of constant dendritic growth velocity, net accelerations of the center of mass of a solidifying system are obtained, irrespective of the precise morphology of the transformation.

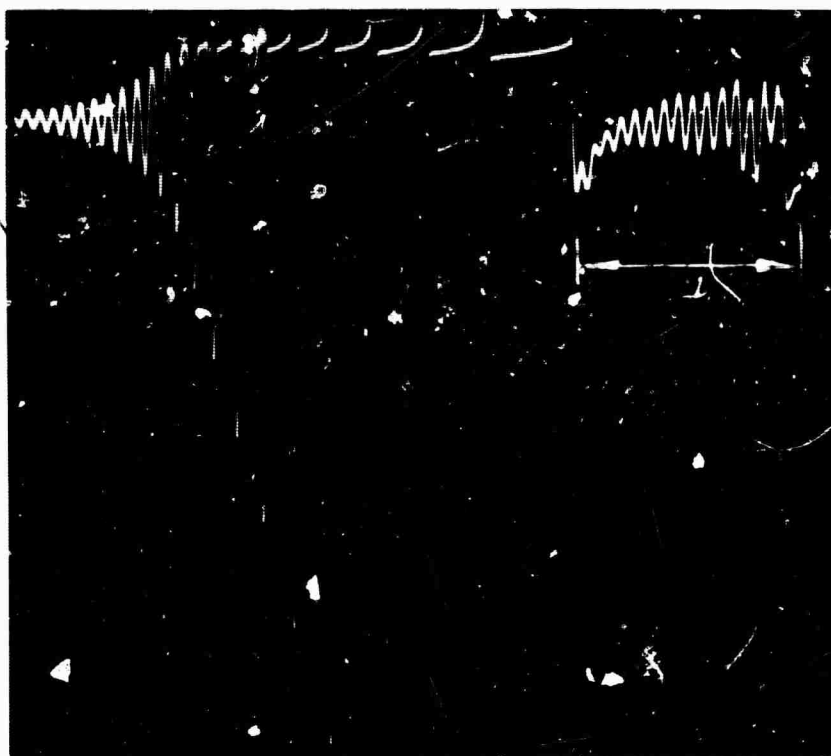


Fig. 16 - Force-time oscillogram obtained from transducer located at the base of a solidifying bismuth specimen. Total horizontal sweep time: 150 msec; vertical deflection sensitivity: 1 volt/cm; approximate force sensitivity: 10^5 dynes/cm.

2. Calculations were made of the momentum acquired during rapid solidification by using a quantitative description of the accelerations of the center of mass along with simplified, but reasonable, dynamical constraints. Thus, it was determined that for free-surface-nucleated systems, the induced momentum increased monotonically over the duration of the transformation, while in the case of base-nucleated systems, a more complicated behavior resulted.

3. The total momentum, or terminal velocity, of the mass center of a solidifying specimen did not vary monotonically with the dendrite growth velocity or with the degree of supercooling. It was found, instead, that the momentum acquired by a specimen achieved a maximum at a level of supercooling which was determined by the material that was freezing and by the value of the maximum net external force provided by the mechanical constraints.

Experiments were then conducted to ascertain the validity of the analysis and to check on the appropriateness of some of the assumptions when applied to real systems. The conclusions given next were derived from these experiments.

1. A cinematographic study of the motion of bismuth dendrites in long (25-cm) capsules verified the assumption that a "forest" of dendrites, nucleated from a single site, can grow for considerable distances at constant speed, with no observable tendency to nucleate crystals ahead of the dendrite tips. Although these observations permit a gross description of the temperature and mass distribution during dendritic growth, the fact that these specimens, in the main, are polycrystalline indicates that the details of this type of solidification are far more complicated than evinced by our observations.

A second mechanism which must be considered is that of the collapse of the surface cavities at the termination of recalescence. When the surface cavities collapse—at least partial collapse must occur at the cessation of dendritic growth—a transient flow of molten metal will be established in the interdendritic channels throughout the specimen. The structure of a specimen just after recalescence is composed of fine (micron diameter), fragile, branched dendrites, which account for about 10 to 50 percent of the volume, and interdendritic melt near the equilibrium temperature, which accounts for the remainder. The presence of fluid flow in such an unstable structure could cause displacements and/or fracture of the dendritic skeleton which would produce a refinement in the final grain size. No enhancement of the nucleation rate is required for this mechanism.

Finally, it appears possible that the impulses, which result when solidification-induced momentum is transferred from a specimen to its surroundings, can interact with the recalesced structure and produce grain refinement. Figure 16 shows the force impulse measured at the base of a crucible of solidifying bismuth. The specimen was supercooled about 85°C when solidification started. The measurements were performed in the same manner as described in the section on experimental work, except that the specimen was not suspended from the accelerometer but rested on an insulating plate to which was attached the force sensor. The photograph shows that the specimen was subjected to two groups of forces: The first group was composed of the solidification-induced forces which lasted about 40×10^{-3} sec, as indicated by the period τ ; the second group consisted of a train of powerful impulses resulting from the transfer, to and fro, of growth-induced momenta between the specimen and the support plate. Impulse pressures as large as 4.2×10^6 dyne/cm² have been measured in bismuth. The linear damping of a portion of the impulses in Fig. 16 indicates that the entire specimen of about 150 gm was subjected to nine or ten restitutive bounces on the support plate. Clearly, then, the evidence is strong for the presence, just after rapid growth ceases, of dendrite-damaging impact pressures. Lastly, it should be noted that the dynamic effects measured when supercooled bismuth solidifies are likely to be considerably milder than those encountered during the solidification of materials such as nickel, iron, or cobalt. The reason is that the maximum growth velocities which are attainable in supercooled bismuth are only about one tenth as large as those observed in the transition metals mentioned above.

SUMMARY AND CONCLUSIONS

A hypothesis has been proposed to explain the dynamical behavior of systems subjected to rapid, dendritic solidification. The theoretical conclusions, given next, were developed from a Newtonian analysis of the mass redistribution which occurs across a dendritic solidification front.

1. It was shown that even under the conditions of constant dendritic growth velocity, net accelerations of the center of mass of a solidifying system are obtained, irrespective of the precise morphology of the transformation.



Fig. 15 - Pitlike surface formations distributed over the base of a cobalt ingot which was supercooled 226°C before solidifying (photograph courtesy of Professor G.A. Colligan, private communication)

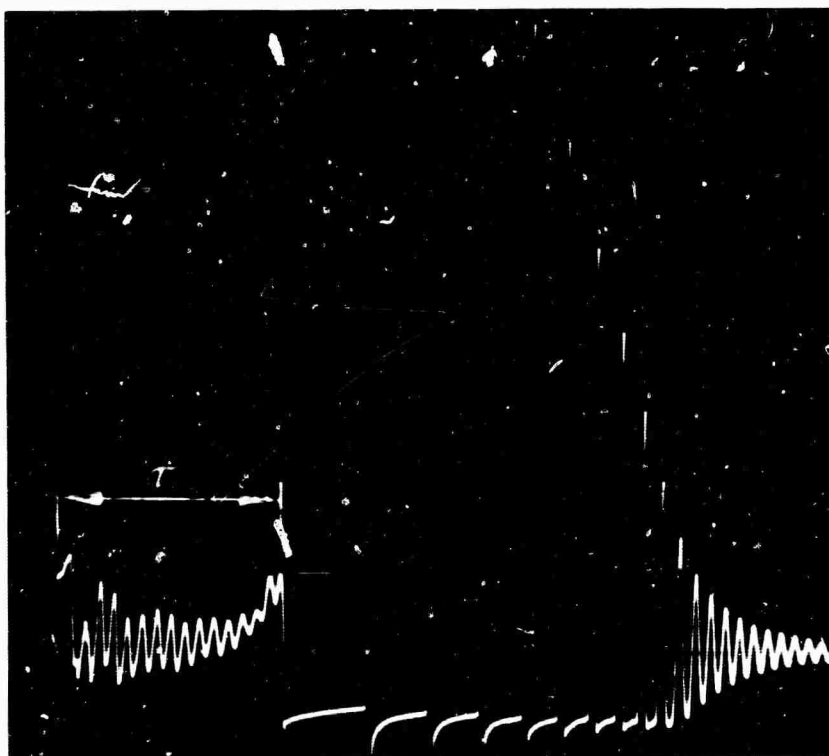


Fig. 16 - Force-time oscillogram obtained from transducer located at the base of a solidifying bismuth specimen. Total horizontal sweep time: 150 msec; vertical deflection sensitivity: 1 volt/cm; approximate force sensitivity: 10^5 dynes/cm.

2. Calculations were made of the momentum acquired during rapid solidification by using a quantitative description of the accelerations of the center of mass along with simplified, but reasonable, dynamical constraints. Thus, it was determined that for free-surface-nucleated systems, the induced momentum increased monotonically over the duration of the transformation, while in the case of base-nucleated systems, a more complicated behavior resulted.

3. The total momentum, or terminal velocity, of the mass center of a solidifying specimen did not vary monotonically with the dendrite growth velocity or with the degree of supercooling. It was found, instead, that the momentum acquired by a specimen achieved a maximum at a level of supercooling which was determined by the material that was freezing and by the value of the maximum net external force provided by the mechanical constraints.

Experiments were then conducted to ascertain the validity of the analysis and to check on the appropriateness of some of the assumptions when applied to real systems. The conclusions given next were derived from these experiments.

1. A cinematographic study of the motion of bismuth dendrites in long (25-cm) capsules verified the assumption that a "forest" of dendrites, nucleated from a single site, can grow for considerable distances at constant speed, with no observable tendency to nucleate crystals ahead of the dendrite tips. Although these observations permit a gross description of the temperature and mass distribution during dendritic growth, the fact that these specimens, in the main, are polycrystalline indicates that the details of this type of solidification are far more complicated than evinced by our observations.

2. A direct confirmation of the qualitative aspects of the dynamical analysis was obtained by measuring the accelerations induced in rapidly solidifying specimens of supercooled bismuth. The form of the acceleration profiles, measured with piezoelectric accelerometers, was in accord with the acceleration profiles predicted from the theory.

3. The momentum acquired by bismuth specimens during their solidification was measured by a method based on the ballistic pendulum principle. Agreement was found between the measured momenta and the theoretically derived values.

4. Pressure pulses between 10^6 and 10^7 dyne/cm² were detected at the termination of recalescence in highly supercooled ($\Delta T \approx 90^\circ\text{C}$) specimens of bismuth. Since the pressure waves within the specimens might have been more intense than those measured, it is concluded that an interaction between the recalesced structure and the solidification-induced impulses is a likely possibility. Moreover, in the solidification of materials such as nickel, iron, and cobalt, wherein dendrite velocities greater than 5000 cm/sec have been observed—compared with the maximum of 500 cm/sec for bismuth—even more intensive dynamic effects are expected than have been measured here.

Finally, it is concluded that a rationale can be provided for explaining several phenomena observed during the rapid solidification of bismuth, nickel, cobalt, and iron. Specifically, interpretations were offered for:

- a. the emission of acoustical disturbances from strongly supercooled melts, during recalescence;
- b. the functional form of the variation (in nickel) of the disturbance amplitude with the degree of supercooling;
- c. the formation of surface pockmarks on rapidly frozen ingots of cobalt, nickel, and iron; and
- d. the transition in grain size which has been observed in cobalt and nickel.

ACKNOWLEDGMENTS

The author is especially indebted to Dr. C.A. Macklitt, Metal Physics Branch, U.S. Naval Research Laboratory, for his stimulating discussions of all phases of this research. In addition, the author owes thanks to Mr. J.L. Walker, General Electric Research Laboratory; to Professor G.A. Colligan, Thayer School, Dartmouth College; and to Mr. B.J. Bayles, United Aircraft Research Laboratory, for giving him access to some of their unpublished results.

Portions of this research were supported by the Materials Science Division of the Advanced Research Projects Agency, and by a National Academy of Sciences-National Research Council Postdoctoral Associateship held by the author at the U.S. Naval Research Laboratory.

REFERENCES

1. Chambré, P.L., *Quart. J. Mech. Appl. Math.* 9:224 (1956)
2. Horvay, G., "Freezing Into an Undercooled Melt Accompanied by a Density Change," General Electric Research Laboratory, Report No. 61-RL-2868M, Schenectady, New York (1961); also, *Int. J. Heat Mass Transfer*, 8:195-243 (1965)
3. Chalmers, B., "Principles of Solidification," p. 104, New York:Wiley (1964)
4. Colligan, G.A., and Bayles, B.J., *Acta Met.*, 10:895 (1962)
5. Walker, J.L., "Physical Chemistry of Process Metallurgy," Part 2, p. 845, George R. St. Pierre, ed., A.I.M.E., New York:Interscience (1961)
6. Walker, J.L., private communication
7. Bayles, B.J., private communication
8. Chalmers, B., "Principles of Solidification," p. 86, New York:Wiley (1964)

TABLE REFERENCES

1. "Metals Handbook," Vol. 1, 8th Ed., p. 47, American Society for Metals, Novelty, Ohio (1961)
2. Kelley, K.K., *Bur. Mines Bull. No. 476*, U.S. Govt. Printing Office, Wash., D.C. (1949)
3. "Liquid Metals Handbook," 2nd Ed., Richard N. Lyon, ed., p. 41, U.S. Govt. Printing Office, Wash., D.C. (1952)
4. Benedicks, C., Ericsson, N., and Ericson, G., *Arch. Eisenhuettenw.* 3(No. 7):473 (1930)
5. Lucas, L.D., *Compt. Rend.* 250:1850 (1960)
3. Enis, A.E., thesis, Rensselaer Polytechnic Institute (1961)